J. Fluid Mech. (1993), *vol.* 250, *pp.* 651–668

Momentum and heat transport in the turbulent intermediate wake of a circular cylinder

By M. MATSUMURA[1] AND R. A. ANTONIA[2]

[1] Department of Applied Mechanical Engineering, Kitami Institute of Technology, Kitami, Hokkaido, 090, Japan

[2] Department of Mechanical Engineering, University of Newcastle, NSW, 2308, Australia

(Received 22 June 1992)

Hot-wire anemometry has been used in the intermediate wake ($x/d = 10$ to 40) of a slightly heated circular cylinder in order to quantify the contribution from the coherent motion to various conventionally averaged quantities, in particular the average momentum and heat fluxes. The overall contribution to the lateral heat flux is always greater than that to the Reynolds shear stress, indicating that the turbulent Kármán vortex street transports heat more effectively than momentum. The difference in these contributions is reflected in the topologies of the velocity and temperature fields. There is significant streamwise evolution of these topologies throughout the intermediate wake. At $x/d = 10$, the net heat transport associated with the vortical motion occurs in the downstream region of each vortex. At other downstream stations, the net heat transport is equally distributed between the upstream and downstream regions of individual vortices.

1. Introduction

The structure of a two-dimensional turbulent wake has received significant attention, prompted mainly by the realization that this flow is characterized by organized or coherent motions. Kiya & Matsumura (1985) and Tritton (1988, p. 333) distinguished between a near wake ($x/d < 4$ or 5), an intermediate wake (5 or $6 < x/d < 50$ or so) and the self-preserving far wake ($x/d >$ several hundred diameters). It is difficult to give precise values for the boundaries between the different regions since they may depend on many parameters, e.g. initial conditions, pressure gradient and Reynolds number. The degree and type of organization may differ significantly among the near, intermediate and far wakes (e.g. Cantwell & Coles 1983; Kiya & Matsumura 1985; Hussain & Hayakawa 1987; Hayakawa & Hussain 1989; Townsend 1979; Mumford 1983; Antonia *et al.* 1987; Cimbala, Naguib & Roshko 1988; Ferré *et al.* 1990). They may also depend on initial conditions, e.g. the type of body which generates the wake (e.g. Kiya & Matsumura 1988; Matsumura *et al.* 1991), or on other parameters (e.g. Reynolds number or pressure gradient). The degree and type of organization should also be reflected in the contribution that the organized motion makes to the Reynolds stresses. There is a high level of organization in the near and intermediate wakes of a circular cylinder, reflecting the presence of the turbulent Kármán vortex street. Accordingly, the contribution from this organization to the normal Reynolds stress $\overline{v^2}$, where v is the lateral velocity fluctuation, is appreciable in these regions (e.g. Kiya & Matsumura, 1985, 1988; Antonia 1991); a smaller, though still significant, contribution to $\overline{v^2}$ is found in the far wake (Antonia *et al.* 1987).

x/d	U_0/U_1	T_0 (°C)	L/d	U_c/U_1
10	0.185	0.687	0.808	0.905
20	0.187	0.426	1.015	0.888
40	0.143	0.333	1.486	0.905

TABLE 1. Velocity defect, temperature excess, half-width and vortex convection velocity at the measurement stations

Although the topology of the velocity field in the near and intermediate wakes has been studied in detail, corresponding investigations of the temperature field have not been made. The present study was undertaken primarily to study the manner in which heat transport is carried out in the intermediate wake and compare it with the momentum transport characteristics. Following the detection of the organized motion by a method based on the lateral velocity fluctuation v, contributions from this motion to the heat and momentum fluxes are quantified and discussed in the context of the topology of the velocity and temperature fields. The results point to significant differences between the manner in which vortices transport momentum and heat. They also indicate significant streamwise variations of the transport characteristics.

2. Experimental details

Measurements were made in an open-return low-turbulence wind tunnel with a working section of 350 mm × 350 mm, 2.4 m long. The wake was generated by a cylinder of diameter $d = 12.6$ mm spanning the width of the working section. The bottom wall of the working section was adjusted to obtain a zero streamwise pressure gradient. The free-stream velocity U_1 was 7 m/s and the Reynolds number, based on U_1 and d, was 5830. Measurements were made in the intermediate wake ($x/d = 10$, 20 and 40, where x is the streamwise distance measured from the cylinder). The cylinder was electrically heated, the amount of heat being sufficiently small for temperature to be considered a passive scalar at all measurement stations. Values of U_0, the velocity defect at the centreline, T_0, the maximum temperature excess (relative to the free-stream ambient temperature) and the half-width L are given in table 1 (see also the definition sketch in figure 1).

For the present experiment, a three-wire probe (combination of X-wire and cold wire, the latter mounted orthogonally to the plane of the X-wire and about 1 mm upstream of the X-wire centre) was used for the measurements of velocity fluctuations u (in the x or streamwise direction), v (in the y-direction) and the temperature fluctuation θ. The three-wire probe was traversed in the y-direction (across the wake) at each station. A single inclined hot wire (fixed at a particular y-value for each measuring station) was also used in conjunction with the three-wire probe in order to provide a phase reference for the signals from the three-wire probe.

The hot wires were made of 5 μm diameter Wollaston (Pt–10% Rh) wire, etched to a length of about 1 mm. The cold wire was etched from a 1.27 μm diameter Wollaston wire, to a length of about 1.1 mm (wire resistance $\approx 160\ \Omega$). The hot wires were operated with in-house constant-temperature circuits at an overheat ratio of 1.8. For the cold wire, a constant-current (0.1 mA) circuit, built in-house, was used. After suitable conditioning, the analogue signals were digitized at a sampling frequency of 6.67 kHz/channel into an NEC 386 personal computer. The digital signals were subsequently transferred via an Ethernet optical cable link to a VAX computer.

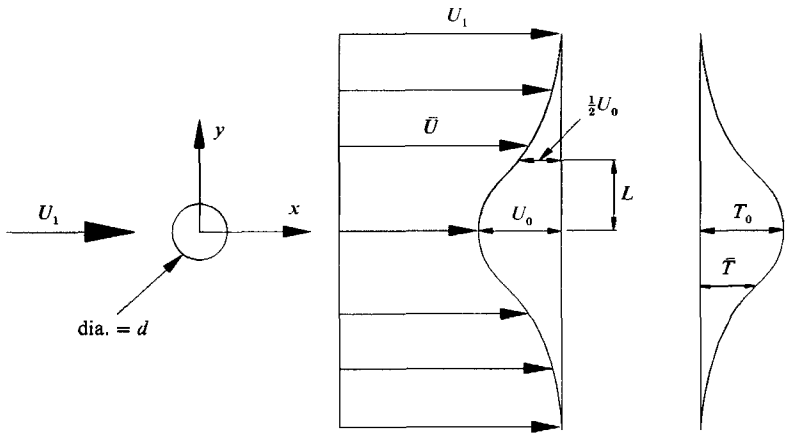

FIGURE 1. Definition sketch.

Velocity and yaw calibrations for the X-wire were carried out in the free stream using a Pitot-static tube connected to a Baratron pressure transducer (with a resolution of about 0.01 mmH_2O). A temperature coefficient of 1.69×10^{-3} °C^{-1} was used for the cold wire.

3. Phase averaging

The phase averaging method is similar to that used by Kiya & Matsumura (1985, 1988) and Matsumura *et al.* (1991). The phase on which the averaging is based is provided by the v-signal from the three-wire probe. This signal was digitally band-pass filtered with the centre frequency of the filter set equal to f_0, the Kármán vortex shedding frequency (the value of f_0, estimated from the frequency at which the v-spectrum was maximum, corresponded to a Strouhal number $f_0 d/U_1$ by about 0.2, independently of x/d). The phase ϕ was then calculated from the filtered signal v_f as follows:

$$\phi = \pi\left(\frac{t-t_{1,i}}{t_{2,i}-t_{1,i}}\right) \quad (t_{1,i} \leqslant t \leqslant t_{2,i}),$$

$$\phi = \pi\left(\frac{t-t_{2,i}}{t_{1,i+1}-t_{2,i}}\right)+\pi, \quad (t_{2,i} \leqslant t < t_{1,i+1}),$$

where $t_{1,i}$ and $t_{2,i}$ correspond to the instants of time (measured from an arbitrary time origin) when $v_f = 0$ and $dv_f/dt > 0$ and when $v_f = 0$ and $dv_f/dt < 0$ respectively. The interval $(t_2 - t_1)$ has an average value of $\frac{1}{2}T_0$ (where $T_0 \equiv f_0^{-1}$), i.e. half the average vortex shedding period. Each interval $(t_2 - t_1)$ was made equal to $\frac{1}{2}T_0$ (by compression or stretching), this half-period being divided into 30 equal intervals. A total of 900 periods was used for the averaging.

The triple decomposition (Reynolds & Hussain 1972) has been applied to instantaneous quantities, i.e.

$$Q = \bar{Q} + \tilde{q} + q_r,$$

where $Q (\equiv U, V \text{ or } T)$ is the instantaneous quantity, $\bar{Q} (\equiv \bar{U}, \bar{V} \text{ or } \bar{T})$ is the time mean (or global) component, $\tilde{q} (\equiv \tilde{u}, \tilde{v} \text{ or } \tilde{\theta})$ is the coherent fluctuation and $q_r (\equiv u_r, v_r \text{ or } \theta_r)$ is the incoherent (or random) fluctuation. The advantages and limitations of the triple decomposition, relative to the double decomposition, have been discussed in detail by

Hussain (1983). The triple decomposition is used here as it enables the contributions from the coherent (and incoherent) motions to the global Reynolds stresses and heat fluxes to be evaluated. Since reliable estimates of these contributions are required, it was important that the signal used for the phase averaging be taken at the measurement point. Using angular brackets to denote phase averaging, $\tilde{q} \equiv \langle q \rangle$ and the phase average of the product qs (where s, like q, represents either u, v or θ) is given by

$$\langle qs \rangle = \tilde{q}\tilde{s} + \langle q_r s_r \rangle.$$

To obtain contours of coherent or incoherent quantities in the (ϕ, y)-plane, a reference phase was used (in conjunction with the local phase). The reference phase was generated from the fixed inclined wire signal by the same method as described above. The difference between the local phase (at each y-location of the three-wire probe) and the reference phase was subsequently used in the contour plots (presented in §5).

4. Coherent contributions to Reynolds stresses and turbulent fluxes

Once the coherent components of the u, v, θ fluctuations (at the moving probe) are obtained by the method outlined in §3, the contributions that the coherent motion makes to the conventional (or global) Reynolds stresses, the temperature variance and the heat fluxes can then be calculated. Distributions across the wake of $\overline{\tilde{q}\tilde{s}}$ (a double overbar denotes averaging over one shedding period) and $\overline{qs}$ (a single overbar denotes conventional or global time averaging) are shown in figures 2 and 3 at the three measurement stations; q and s represent either u, v or θ. Here and elsewhere, an asterisk denotes normalization† by either U_0, the half-width L or T_0 (these quantities are defined in figure 1).

Figure 2 shows that the coherent motion makes a more important contribution to $\overline{v^2}$ than to either $\overline{u^2}$ or $\overline{\theta^2}$. The distributions of $\overline{\tilde{v}^2}$ and $\overline{v^2}$ are quite similar in shape and magnitude at all three stations. Note that $\overline{\tilde{u}^2}$ is nearly zero on the wake centreline, with local maxima on either side of the centreline. The magnitude of these peaks is especially pronounced at $x/d = 10$, where relatively minor peaks are also seen in $\overline{u^2}$. The distributions of $\overline{\tilde{\theta}_2}$ and $\overline{\theta^2}$ are double peaked at $x/d = 20$ and 40, the double peak in $\overline{\theta^2}$ being quite strong at $x/d = 40$. The coherent contributions to $\overline{u^2}$ and $\overline{\theta^2}$ are quite small at $x/d = 20$ and 40. It should be noted however that the present detection method focuses on v, and contributions to $\overline{u^2}$ and $\overline{\theta^2}$ are likely to be underestimated relative to $\overline{v^2}$. As x/d increases, the periodicity of the velocity (and temperature) fluctuations weakens and, at $x/d = 40$, quantities such as $\overline{\tilde{u}^2}$ and $\overline{\tilde{u}\tilde{v}}$ should be less reliable than $\overline{\tilde{v}}$ or $\overline{\tilde{v}\tilde{\theta}}$. The results presented in this section should be viewed with this qualification in mind.

The distribution of $\overline{\tilde{v}\tilde{\theta}}$ has the same sign as that of $\overline{v\theta}$ at all three stations (figure 3). This trend is also valid for the other two fluxes at $x/d = 10$ and 40 but does not apply at $x/d = 20$. At this latter station, $\overline{\tilde{u}\tilde{v}}$ exhibits a small positive local maximum near $y^* \approx 1.4$ ($\overline{uv}$ is negative there but its magnitude is larger than that of $\overline{\tilde{u}\tilde{v}}$) and a small negative local minimum at $y^* \approx -1.4$ (where $\overline{uv}$ is positive). This behaviour implies that the vortical motion can yield a Reynolds shear stress with a sign opposite to that of $\overline{uv}$. The tendency of the vortical motion to reduce the level of $\overline{uv}$ is also seen at $x/d = 10$ (near $|y^*| \approx 1.4$) but there is no sign change in $\overline{\tilde{u}\tilde{v}}$ at this station. At $x/d = 20$,

† This normalization is used for convenience since the velocity and temperature fields in the intermediate wake are not self-preserving. This lack of self-preservation will clearly be reflected in the topological results of §5.

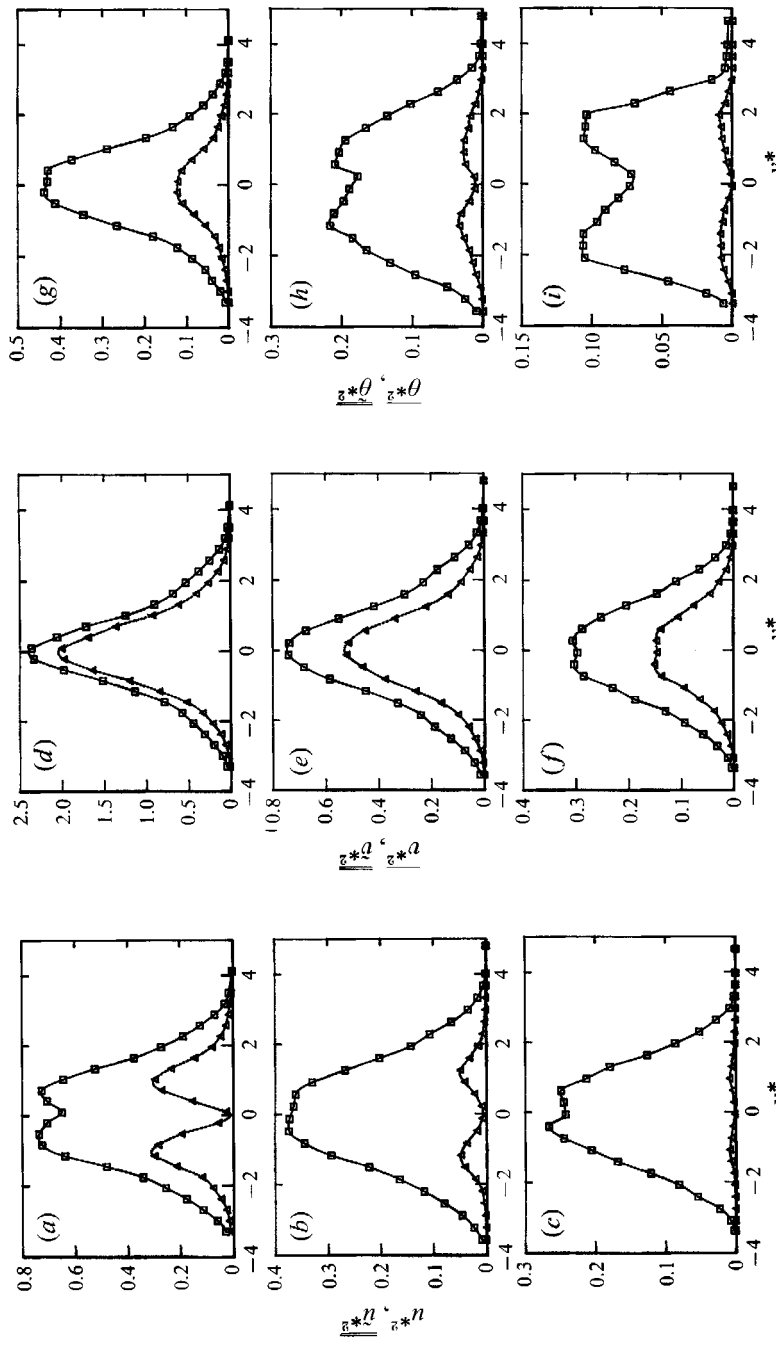

FIGURE 2. Global and coherent Reynolds normal stresses and temperature variance. □, global; △, coherent. u^{*2}: (*a*) $x/d = 10$; (*b*) $x/d = 20$; (*c*) $x/d = 40$; v^{*2}: (*d*) $x/d = 10$; (*e*) $x/d = 20$; (*f*) $x/d = 40$; θ^{*2}: (*g*) $x/d = 10$; (*h*) $x/d = 20$; (*i*) $x/d = 40$.

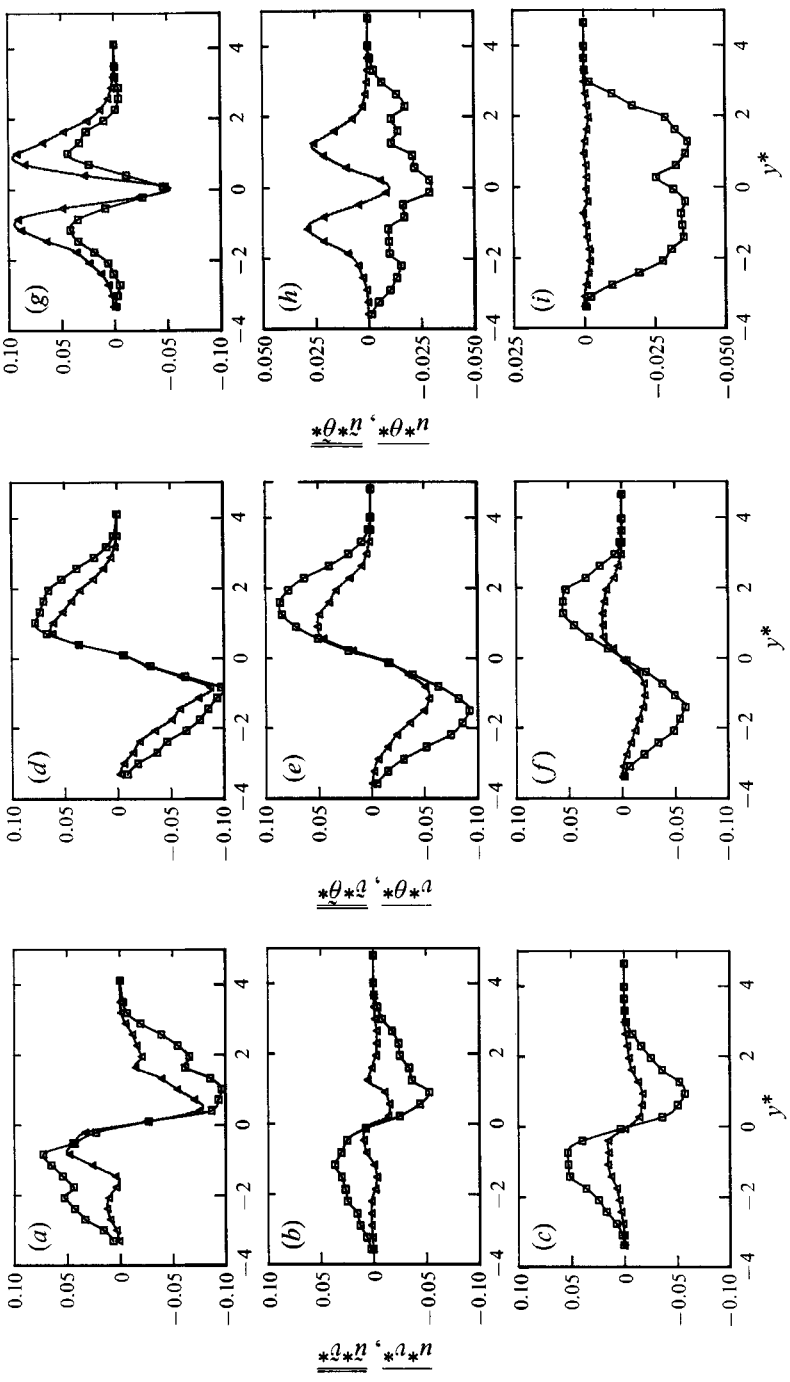

FIGURE 3. Global and coherent Reynolds shear stress and heat fluxes. □, global; △, coherent. u^*v^*: (*a*) $x/d = 10$; (*b*) $x/d = 20$; (*c*) $x/d = 40$; $v^*\theta^*$: (*d*) $x/d = 10$; (*e*) $x/d = 20$; (*f*) $x/d = 40$; $u^*\theta^*$: (*g*) $x/d = 10$; (*h*) $x/d = 20$; (*i*) $x/d = 40$.

		10			20			40		
x/d										
q	s	S_c	S_g	f(%)	S_c	S_g	f(%)	S_c	S_g	f(%)
u	u	0.821	2.66	30.9	0.131	1.36	9.6	0.0214	0.878	2.4
v	v	4.49	6.11	73.4	1.33	2.33	57.0	0.418	1.03	40.6
θ	θ	0.291	1.251	23.3	0.110	0.960	11.4	0.0318	0.510	6.2
u	v	0.164	0.338	48.5	0.0325	0.169	19.2	0.0519	0.193	26.9
v	θ	0.240	0.353	68.0	0.194	0.373	51.9	0.0750	0.221	34.0
u	θ	0.253	0.119	213.0	0.0675	0.0979	68.9	0.0051	0.162	3.1

TABLE 2. Averaged contributions from the coherent motion to the Reynolds stresses, heat fluxes and temperature variance

$\overline{\tilde{u}\tilde{\theta}}$ is of opposite sign to $\overline{u\theta}$, except near the centreline. Clearly, the organized motion acts in a way that reduces the magnitude of $\overline{u\theta}$ at this station (this is especially noticeable in the region $1 \lesssim |y^*| < 2$). It is of interest to note that the positive peaks in $\overline{\tilde{u}\tilde{\theta}}$ at $x/d = 10$ are twice as large as those in $\overline{u\theta}$, implying a large negative contribution from the incoherent or random motion. Except near the centreline, $\overline{u\theta}$ is positive at $x/d = 10$, in contrast to the negative distributions of $\overline{u\theta}$ at $x/d = 20$ and 40 and in the far wake (e.g. Fabris 1979; Antonia & Browne 1986). The negative value of $\overline{u\theta}$ near the centreline at $x/d = 10$ is approximately equal to $\overline{\tilde{u}\tilde{\theta}}$ and is therefore provided almost entirely by the organized motion associated with the strong vortices. There is practically no contribution from the organized motion to $\overline{u\theta}$ at $x/d = 40$.

One way of assessing the streamwise variation of the coherent contribution is to consider the dependence of the ratio $\overline{\tilde{q}\tilde{s}}/\overline{qs}$ on x/d. Since this ratio also depends on y^*, we have chosen to compute an averaged contribution, across the wake, from the coherent motion. For this purpose, the ratio

$$f = S_c/S_g$$

is introduced, where

$$S_c = \int_{-Y^*}^{Y^*} |\overline{\tilde{q}\tilde{s}}|\,\mathrm{d}y^*, \qquad S_g = \int_{-Y^*}^{Y^*} |\overline{qs}|\,\mathrm{d}y^*,$$

Y^* denoting the position at which $|\overline{qs}|$ is nearly zero. Absolute values are used in S_c and S_g to allow for changes in sign of the fluxes. The values of f, shown in table 2, suggest the following comments:

(i) The coherent contribution to $\overline{v^2}$ is greater than that to any of the other Reynolds stresses. At $x/d = 40$, it is significantly larger than the contributions to any of the other quantities. This strong contribution to $\overline{v^2}$, previously reported by Kiya & Matsumura (1985) and Antonia (1991), reflects the enhancement of $\tilde{v}$ due to the primarily antisymmetrical arrangement of the counter-rotating vortices of the Kármán street.

(ii) At $x/d = 10$ and 20, the largest value of f relates to $\overline{u\theta}$. Consistent with figure 3, f is exceptionally large (more than 200%) at $x/d = 10$ while it is negligible at $x/d = 40$.

(iii) Contributions to $\overline{uv}$ and $\overline{v\theta}$ are significant at all stations but the contribution to $\overline{v\theta}$ is always larger than that to $\overline{uv}$. It should be noted that the coherent contribution to $\overline{uv}$ is smaller at $x/d = 20$ than at either $x/d = 10$ or 40. This result is consistent with the changes in sign of $\overline{\tilde{u}\tilde{v}}$ at $x/d = 20$.

The small value of f for uv at $x/d = 20$, relative to that for $v\theta$, implies that momentum transport is severely hampered by comparison to heat transport. Estimates

of the turbulent Prandtl number $Pr_T \equiv (\overline{uv}/\partial\bar{U}/\partial y)/(\overline{v\theta}/\partial\bar{T}/\partial y)$ support this implication. Approximate values of Pr_T, averaged across the wake, were 0.9, 0.4 and 0.8 at $x/d = 10$, 20 and 40 respectively.

5. Topology of velocity and temperature fields

Contours of quantities associated with the coherent and random motions are shown in the (ϕ, y^*)-plane, where the phase $\phi(-2\pi$ to $+2\pi)$ can also be interpreted in terms of a streamwise distance ($\phi = 2\pi$ corresponds to the Kármán wavelength $T_0 U_c$ where U_c is the convection velocity of the vortices). Note that the same scales are used in the ϕ- and y^*-directions in order to avoid any distortion of the physical space. Estimates of U_c, identified with the values of $\bar{U}+\tilde{u}$ at the vortex centres, are given in table 1.

Isocontours of the coherent (phase-averaged) spanwise vorticity $\tilde{\omega} \equiv \partial(\bar{V}+\tilde{v})/\partial x - \partial(\bar{U}+\tilde{u})/\partial y$, where $\partial/\partial x \equiv -U_c^{-1}\partial/\partial t$ are shown in figure 4(*a–c*). Contours of the phase-averaged temperature $\bar{T}+\tilde{\theta}$ are shown in figure 4(*d–f*). The positions of centres (or foci) and saddle points are denoted by C and S respectively. (The location of these critical points was inferred from velocity vector plots in a frame of reference which translates with the vortices.) In figure 4 and in subsequent figures, the flow direction is left to right. At $x/d = 10$, there is a close similarity between the strong $\bar{T}+\tilde{\theta}$ contours and the large-$\tilde{\omega}$ contours. It is clear however that this correspondence weakens as x/d increases, although local maxima of $\bar{T}+\tilde{\theta}$ at $x/d = 20$ and 40 coincide approximately with the peak values of $|\tilde{\omega}|$. There is significant distortion of the $\tilde{\omega}$ contours between $x/d = 10$ and 40, consistent with previous observations (e.g. Hussain & Hayakawa 1987). At $x/d = 10$, the smaller-valued isotherms are drawn in towards the centreline on the downstream side of individual vortices, thus reflecting the arrival of relatively cold fluid in the space (or alleyway) between adjacent vortices. As x/d increases, the asymmetry is less pronounced and has nearly disappeared at $x/d = 40$. At the latter station, the low-valued isotherms suggest the presence of relatively cold fluid on either side of each vortex. The diverging separatrices are shown in figure 4 as broken lines passing through the saddle points. In the far wake (Antonia *et al.* 1987; Ferré and Giralt 1989), the diverging separatrices correspond approximately to the temperature fronts (the temperature gradient in a direction normal to the front is quite large). This correspondence does not seem to apply here (especially at $x/d = 10$ and 20) where the separatrices intersect the isotherms and the temperature gradient in a direction normal to the separatrix is not especially large except where the separatrix joins up with the outer boundaries of the vortices. Instantaneous temperature traces at $x/d = 10$ suggest that the intermittency factor is everywhere smaller than unity (this is consistent with the near-wake intermittency factor measurements of Cantwell & Coles 1983 and Boisson, Chassaing & Ha Minh 1983) so that large temperature gradients should occur primarily across the outer boundaries of the vortices.

The lack of symmetry in the temperature contours (figure 4*d*, $x/d = 10$) is emphasized in the contours of $\tilde{\theta}$ (figure 5*c*), the latter being in clear contrast to the nearly symmetrical $\tilde{u}$ (figure 5*a*) and $\tilde{v}$ (figure 5*b*) contours. The appearance of the $\tilde{u}$ and $\tilde{v}$ contours is similar to that previously reported (Kiya & Matsumura 1985; Hussain & Hayakawa 1987; Antonia 1991) and need not be discussed further. The pronounced asymmetry (with respect to $\phi = 0$) of the $\tilde{\theta}$ contours (centred on the alleyways between vortices) reflects the temperature differences between the regions immediately upstream and downstream of individual vortices. For example, the $\tilde{\theta}$ contours centred on the vortex at $\phi = 0$ are flanked by negative contours but the downstream contours are more negative than the upstream ones since they are

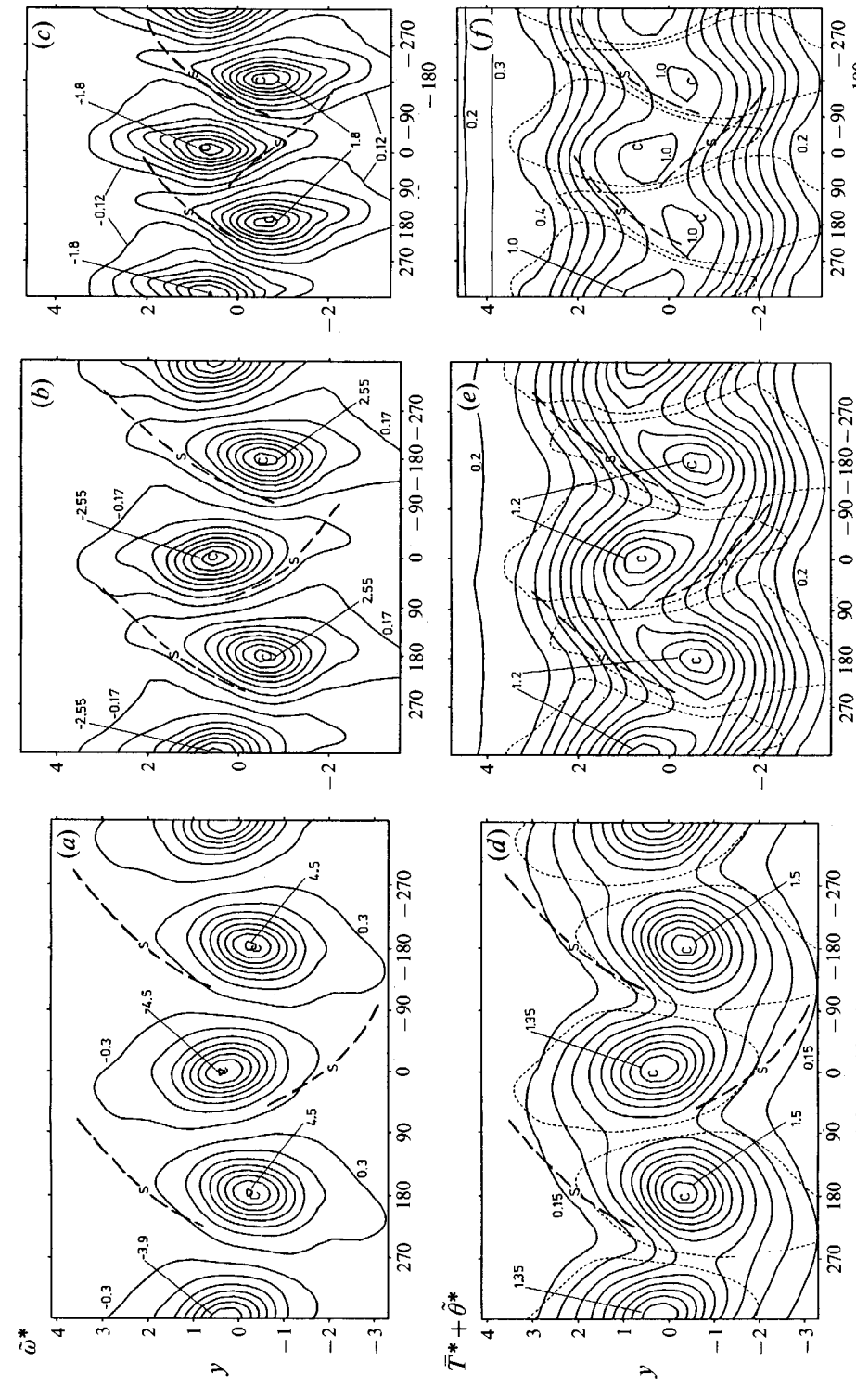

FIGURE 4. Phase-averaged spanwise vorticity and temperature contours. (*a–c*) $\tilde{\omega}^*$ (contour intervals = 0.6, 0.34, 0.24 at $x/d = 10$, 20, 40 respectively). (*d–f*) $\bar{T}^*+\tilde{\theta}^*$ (contour intervals = 0.15, 0.10, 0.10 at $x/d = 10$, 20, 40 respectively). The outermost vorticity contours in (*a–c*) are shown in (*d–f*). Centres and saddles are denoted by C and S. The broken line which pass through S are the diverging separatrices. Here and in subsequent figures, the dashed line denote 5% maximum or 5% minimum vorticity contours.

x/d	$\tilde{\omega}^*_{\max}$	$\tilde{\omega}^*_{\min}$
10	4.626	−4.553
20	2.712	−2.782
40	1.951	−1.942

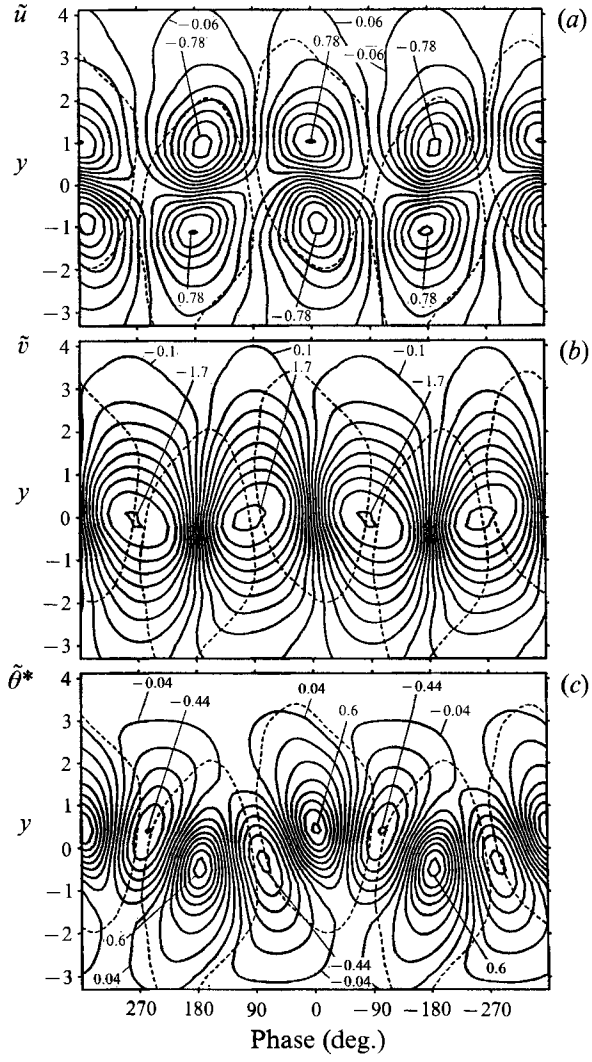

FIGURE 5. Contours of phase-averaged velocity and temperature fluctuations at $x/d = 10$. (*a*) $\tilde{u}^*$; (*b*) $\tilde{v}^*$; (*c*) $\tilde{\theta}^*$. Contour intervals are 0.12, 0.2 and 0.08 for (*a*), (*b*) and (*c*) respectively.

associated with fluid which originated in the free stream on the same side of the centreline as the vortex. Although not shown here, the symmetry in θ decreases when x/d increases, a trend consistent with the behaviour of $\bar{T}+\tilde{\theta}$ in figure 4(*d–f*).

Contours of coherent momentum and heat fluxes are shown in figure 6 while contours of the random fluxes are presented in figure 7. A number of comments can be made with respect to the changes that can be observed between $x/d = 10$ and 40. In general, these variations are more pronounced for coherent than for random quantities. While there are marked differences between $\tilde{u}\tilde{v}$ (figure 6*a*), $\tilde{v}\tilde{\theta}$ (figure 6*d*) and $\tilde{u}\tilde{\theta}$ (figure 6*g*) at $x/d = 10$, these quantities are much more similar in appearance at $x/d = 40$ (figure 6*c*, *f*, *i*). In particular, the similarity between $\tilde{u}\tilde{v}$ (figure 6*c*) and $\tilde{v}\tilde{\theta}$ (figure 6*f*) at $x/d = 40$ is consistent with the relative closeness in the coherent contributions to $\overline{uv}$ and $\overline{v\theta}$ at this station (table 2). The streamwise variation in $\tilde{u}\tilde{\theta}$ is more evident than for the other two fluxes, consistent with the major changes that occur in $\overline{u\theta}$ (figure 3) between $x/d = 10$ and 40. At $x/d = 40$, successive $\tilde{u}\tilde{\theta}$ contours (on

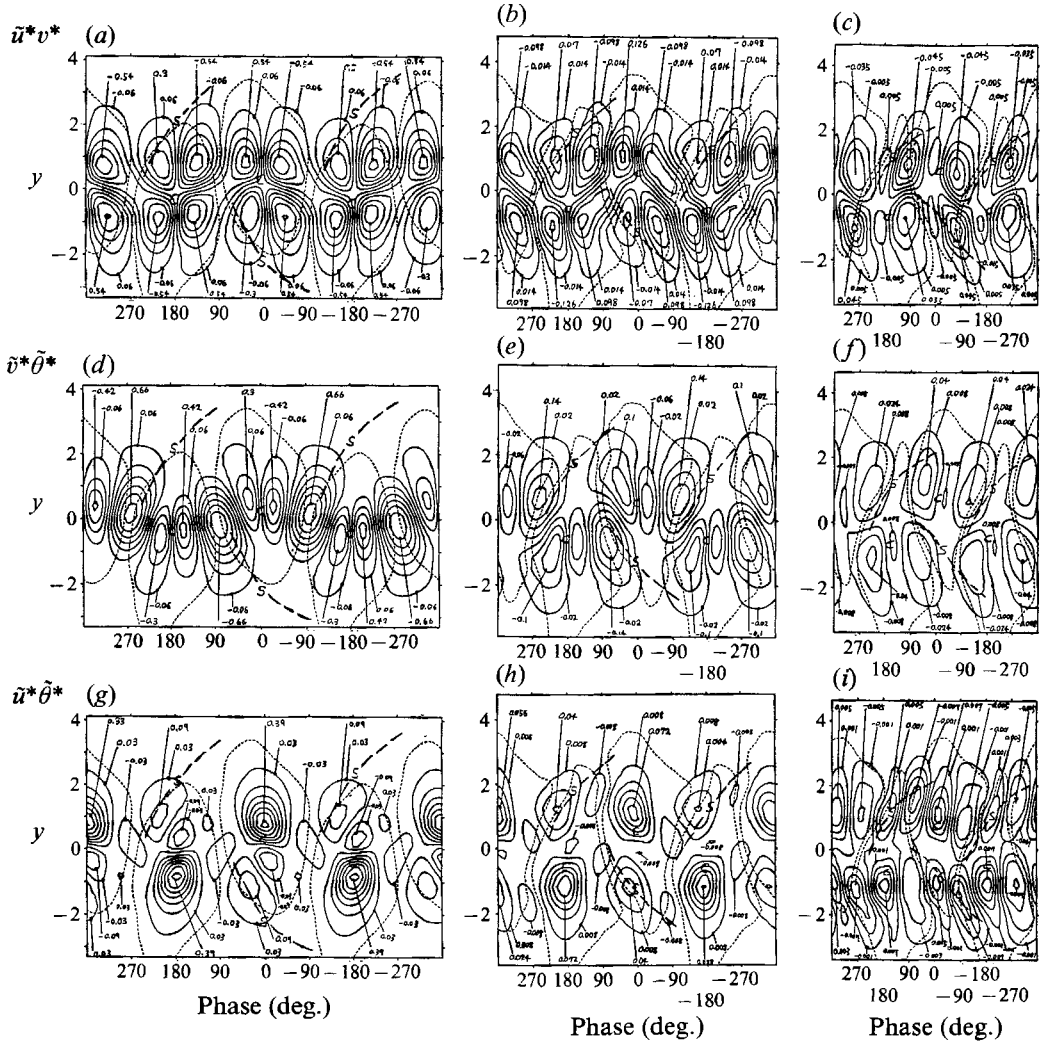

FIGURE 6. Contours of phase-averaged coherent momentum and heat fluxes. $\tilde{u}^*\tilde{v}^*$: (*a*) $x/d = 10$; (*b*) $x/d = 20$; (*c*) $x/d = 40$. $\tilde{v}^*\tilde{\theta}^*$: (*d*) $x/d = 10$; (*e*) $x/d = 20$; (*f*) $x/d = 40$. $\tilde{u}^*\tilde{\theta}^*$: (*g*) $x/d = 10$; (*h*) $x/d = 20$; (*i*) $x/d = 40$. Contour intervals are 0.12, 0.028 and 0.01 for (*a*), (*b*) and (*c*) respectively. Contour intervals are 0.12, 0.04 and 0.016 for (*d*), (*e*) and (*f*) respectively. Contour intervals are 0.06, 0.016 and 0.002 for (*g*), (*h*) and (*i*) respectively.

either side of the centreline) alternate in sign but their size and magnitude are nearly the same, accounting for the virtual disppearance of the coherent contribution to $\overline{u\theta}$ (table 2).

Although the $\tilde{u}\tilde{v}$ contours at $x/d = 10$ (figure 6*a*) and $x/d = 20$ (figure 6*b*) are nearly symmetrical about $\phi = 0$, the small departure from symmetry is sufficient to yield a non-negligible contribution to $\overline{uv}$. (Perfect symmetry about $\phi = 0$ would result in a zero contribution since the sign of $\tilde{u}\tilde{v}$ changes from one set of contours to the adjacent set.) In the case of $\tilde{v}\tilde{\theta}$ (figure 6*d*, *e*) the positive contours extend to larger positive y^* than negative contours. This trend becomes more pronounced as x/d increases. For $y^* > 0$, the negative-$\tilde{v}\tilde{\theta}$ contours have practically disappeared at $x/d = 40$ (figure 6*f*). This seems reasonable as negative-$\tilde{v}\tilde{\theta}$ regions would not be expected to survive where $\partial\bar{T}/\partial y$ is negative; consistently, positive-$\tilde{u}\tilde{v}$ regions disappear where $\partial\bar{U}/\partial y$ is positive, as

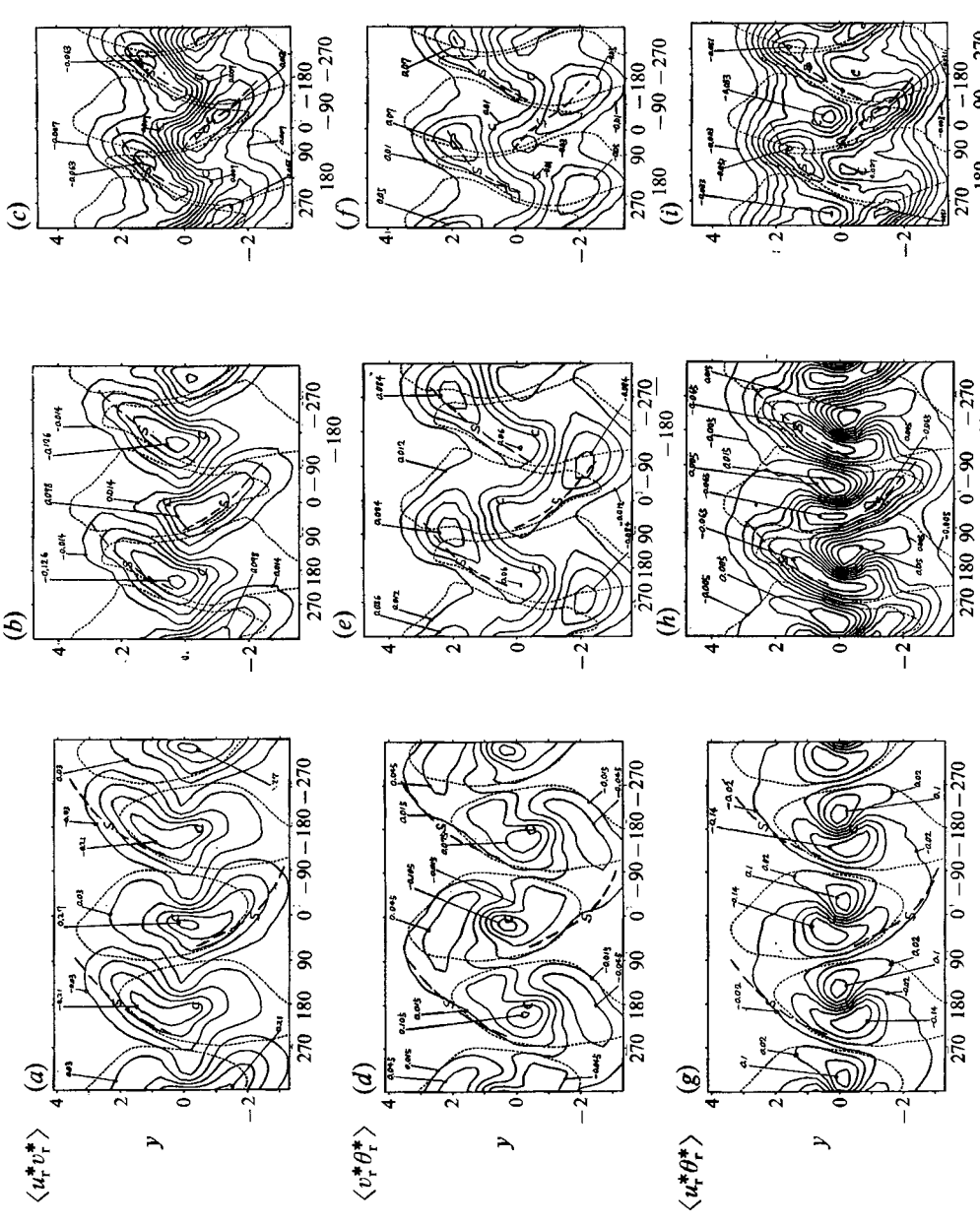

FIGURE 7. Contours of phase-averaged random momentum and heat fluxes. $\langle u_r^* v_r^* \rangle$: (*a*) $x/d = 10$; (*b*) $x/d = 20$; (*c*) $x/d = 40$. $\langle v_r^* \theta_r^* \rangle$: (*d*) $x/d = 10$; (*e*) $x/d = 20$; (*f*) $x/d = 40$. $\langle u_r^* \theta_r^* \rangle$: (*g*) $x/d = 10$; (*h*) $x/d = 20$; (*i*) $x/d = 40$. Contour intervals are 0.06, 0.028 and 0.014 for (*a*), (*b*) and (*c*) respectively. Contour intervals are 0.03, 0.024 and 0.02 for (*d*), (*e*) and (*f*) respectively. Contour intervals are 0.04, 0.01 and 0.006 for (*g*), (*h*) and (*i*) respectively.

illustrated by figure 6(*c*). Figure 6 is fully consistent with the previous conclusion (§4) that the coherent motion makes a larger contribution to $\overline{v\theta}$ than to $\overline{uv}$. At $x/d = 10$, the positive $\tilde{u}\tilde{v}$ contours are dominant on either side of the centreline, in conformity with the overwhelmingly large contribution to $\overline{u\theta}$ reported in table 2. Near the centreline, there are several negative contours, consistent with the conspicuously negative values of $\overline{u\theta}$ near $y = 0$ at $x/d = 10$ (figure 3*g*). Note that negative contours start to appear at $x/d = 20$, in the region between the more important positive contours. At $x/d = 40$, the negative contours are comparable, both in magnitude and extent, to the positive contours.

As expected, contours of $\langle u_r v_r \rangle$, $\langle v_r \theta_r \rangle$ and $\langle u_r \theta_r \rangle$ (figure 7*b*) are significantly different from the corresponding coherent flux contours of figure 6. For example, at $x/d = 10$, the extrema of $\langle u_r v_r \rangle$ (figure 7*a*) and $\langle v_r \theta_r \rangle$ (figure 7*d*) occur near the centres (or foci) but these contours, especially $\langle u_r v_r \rangle$, are stretched in the direction of the diverging separatrix; this behaviour is in marked contrast to the $\tilde{u}\tilde{v}$ and $\tilde{v}\tilde{\theta}$ patterns at this station. Note that $\langle u_r v_r \rangle$ is everywhere positive in the vortices above the centreline and negative in those below the centreline. As x/d increases, the extrema of $\langle u_r v_r \rangle$ and $\langle v_r \theta_r \rangle$ move away from the centres and tend to occur in the space between neighbouring vortices. For $y > 0$, the positive $\langle u_r v_r \rangle$ regions have practically disappeared at $x/d = 40$ and the concentration of negative $\langle u_r v_r \rangle$ is very near the saddle points. At $x/d = 10$, the $\langle u_r \theta_r \rangle$ patterns (figure 7*g*) are concentrated on either side of the centreline, positive and negative extrema of approximately equal magnitude occurring in pairs on either side of a centre; the net contribution to $\overline{u\theta}$ should therefore be negligible, as is implied by the equality between $\overline{\tilde{u}\tilde{\theta}}$ and $\overline{u\theta}$ at $y^* = 0$ (figure 3*g*).

6. Transport of heat: discussion

An effective way of viewing the transport of heat associated with the vortical motion is to plot the heat flux vectors $\tilde{\boldsymbol{q}}$ and $\langle \boldsymbol{q}_r \rangle$ (figure 8). Both the coherent $\tilde{\boldsymbol{q}}$ ($\equiv i\tilde{u}\tilde{\theta} + j\tilde{v}\tilde{\theta}$ where $\boldsymbol{i}$ and $\boldsymbol{j}$ are unit vectors in the x- and y-directions respectively) and random $\tilde{\boldsymbol{q}}_r$ ($\equiv \boldsymbol{i}\langle u_r \theta_r \rangle + \boldsymbol{j}\langle v_r \theta_r \rangle$) vectors are shown together with the velocity vectors† $V - V_c$ (components $\bar{U} + \tilde{u} - U_c, \tilde{v} + \bar{V}$) in a frame of reference which translates with a velocity equal to U_c. (Note that each vector is a projection in the (ϕ, y^*)-plane of the total velocity vector since the spanwise velocity fluctuation w was not measured.)

In the neighbourhood of the vortex centre at $x/d = 10$ (figure 8*d*), $\tilde{q}$ is significant and appears to be proportional to the velocity vector $(V - V_c)$. This behaviour is discernible at $x/d = 20$ but is absent at $x/d = 40$, reflecting the considerable weakening of the vortices at this station. It would seem that the coherent motion within the vortex does not contribute to any net transport of heat out of the vortex. At $x/d = 10$, the magnitude of $\tilde{\boldsymbol{q}}$ is quite small for $|y^*| \gtrsim 1$ (note $\tilde{\boldsymbol{q}}$ changes sign at $|y^*| \approx 1$) immediately upstream of individual vortices and approximately in alignment with the velocity vectors (i.e. positive v is associated with positive, albeit weak, θ). As x/d increases, the location where $\tilde{\boldsymbol{q}}$ changes sign moves towards the centreline (at $x/d = 40$, it is virtually at $y^* = 0$) and the magnitude of $\tilde{\boldsymbol{q}}$ is approximately equal on either side of this location. This is partly because individual vortices are moving away from the centreline and the induced motion upstream of the vortices now carries warmer fluid than at $x/d = 10$. At $x/d = 40$, the $\tilde{\boldsymbol{q}}$ patterns are relatively simple. They are symmetrical about $y = 0$; $\tilde{\boldsymbol{q}}$ is aligned in either the $+y$ or $-y$ directions and its magnitude is significantly only in the alleyways.

† The mean lateral velocity $\bar{V}$ is less than $0.01\bar{U}$ and may be neglected. The lateral velocity V_c at the centre of the vortex is also neglected.

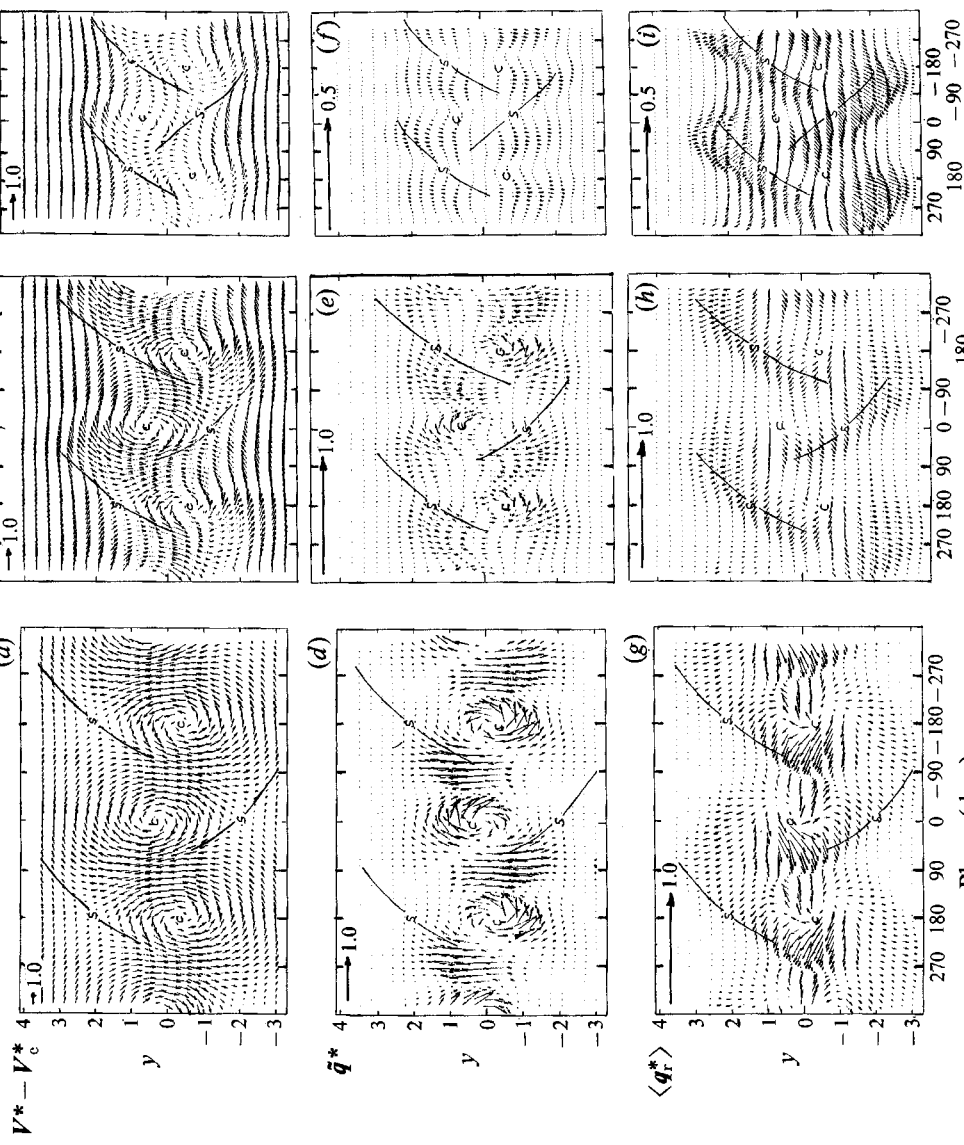

FIGURE 8. Phase-averaged coherent and random heat flux vectors. Also shown are phase-averaged velocity vectors (in a reference frame which translates at a convection velocity U_c). $\boldsymbol{V}^* - \boldsymbol{V}_c^*$: (*a*) $x/d = 10$; (*b*) $x/d = 20$; (*c*) $x/d = 40$. $\tilde{\boldsymbol{q}}^*$: (*d*) $x/d = 10$; (*e*) $x/d = 20$; (*f*) $x/d = 40$. $\langle \boldsymbol{q}_r^* \rangle$: (*g*) $x/d = 10$; (*h*) $x/d = 20$; (*i*) $x/d = 40$. The magnitudes of the vectors are indicated by the size of the arrow at the top left corner of each part of the figure.

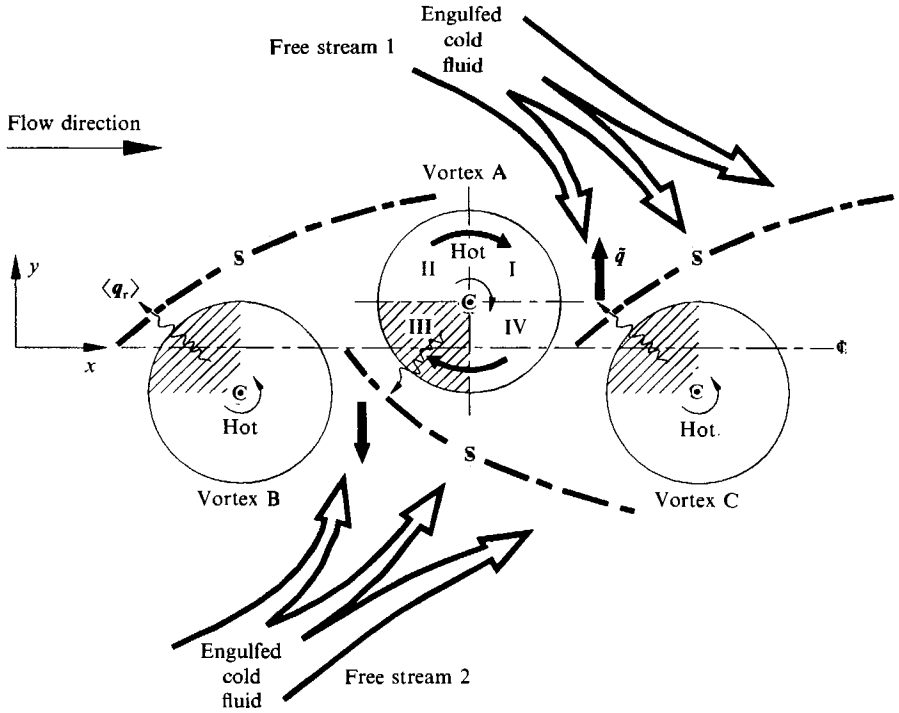

FIGURE 9. Summary sketch of topology at $x/d = 10$.

Unlike $\tilde{q}$, $\langle q_r \rangle$ (figure 8) has a significant streamwise component and generally points upstream. The magnitude of $\langle q_r \rangle$ is generally large near the diverging separatrices and its direction is approximately normal to the separatrices.

With the qualification that the present topological information is only two-dimensional, some general comments can be made on how momentum and heat are transported by the vortices and how this transport evolves in the streamwise direction. For convenience, the discussion will focus mainly on vortex A in figure 9 which is a simplified summary of the topology at $x/d = 10$. There is strong engulfment of potential fluid from free stream 1 on the downstream side of vortex A. It is quite likely (as noted by Cantwell & Coles 1983 and Hussain & Hayakawa 1987) that potential fluid from free stream 2 (on the opposite side of the centreline) is also drawn into the alleyway upstream of vortex A (due to the combined action of vortices B and A).

The rotational (coherent) motion within vortex A does not seem to contribute to the net† transport of heat out of the vortex. The engulfment of cold air (free stream 1) contributes, however, to the transport of heat (away from the centreline) in the downstream alleyway.

The transfer of heat out of the vortex centre (where the temperature is highest) appears to be due to the incoherent motion. There is significant incoherent heat transport directed mainly (though not exclusively) upstream of the vortex centre (figure 8*g*), consistent with the relatively large negative values of $\langle u_r \theta_r \rangle$ (figure 7*g*). It would appear that this is strongly linked with the arrival of cold fluid (free stream 2) due to vortex B. Some of this fluid is assimilated into vortex A, the most likely place being quadrant III, where the local velocity, in a frame of reference which moves with the

† It must of course contribute locally to heat transfer; e.g. at or near the centreline, it contributes almost entirely to $-\overline{u\theta}$.

vortices, is low. This would account for the signs of $\langle u_r v_r \rangle$ (positive), $\langle v_r \theta_r \rangle$ (negative) and $\langle u_r \theta_r \rangle$ (negative) in this quadrant. This may also explain why the magnitude of $\tilde{u}\tilde{v}$ is weaker in quadrant III than the other quadrants (figure 6*a*). It is pertinent here to comment on the role of the saddle point; one expects the local strain rate and $\langle u_r v_r \rangle$ to be high there, thus resulting in a large turbulent energy production. As noted earlier, the $\langle u_r v_r \rangle$ (also $\langle u_r \theta_r \rangle$ and $\langle v_r \theta_r \rangle$) contours are stretched towards the saddle point location. However, the peak value of these quantities occur near the centre and not the saddle point. This result differs from that of Cantwell & Coles (1983) or Hussain & Hayakawa (1987) (the latter result being more applicable at $x/d = 40$). In the near wake and initial part of the intermediate wake, relatively important incoherent Reynolds shear stresses and heat fluxes reside within the vortical region (this is as it should be, given the intermittent nature of the flow).

As x/d increases, the strength of the vortex decays and the jitter in its location and shape increases. Between $x/d = 10$ and 40, the peak vorticity, normalized by U_1 and d, decreases by a factor of about 6 while the circulation decreases by a factor of 2. The normalized peak vorticity values (1.06, 0.50, 0.19 at $x/d = 10$, 20, 40 respectively) are in good agreement with those reported in figure 3 by Hayakawa & Hussain's (1989) paper. The streamwise variations in the vortex characteristics are accompanied by the disappearance of the positive $\tilde{u}\tilde{v}$, $\langle u_r v_r \rangle$ and of the negative $\tilde{v}\tilde{\theta}$, $\langle v_r \theta_r \rangle$ contours. The incoherent motion now plays a more dominant role in the transfer of heat and momentum. The dynamical importance of the region along the diverging separatrix also increases. Figure 7 shows that the extrema in $\langle u_r v_r \rangle$ and $\langle v_r \theta_r \rangle$ move away from the centres towards the space between neighbouring vortices. Many features of the topology at $x/d = 40$ are similar to those in the far wake (Antonia *et al.* 1987). Hayakawa & Hussain (1989) concluded that the organized structures in the nominally two-dimensional wake exhibit significant three-dimensionality even in the near field. It seems reasonable to assume that this three-dimensionality becomes more pronounced as x/d increases; this would be consistent with the previous suggestion of the enhanced role of the diverging separatrix (along which the rib-like vortices are aligned) with increasing x/d. While the present investigation has only considered two-dimensional aspects of the flow, it would clearly be of interest in the future to examine momentum and heat transfer characteristics in the context of the three-dimensional organization.

It is worth commenting on the sudden decrease in the coherent momentum transport at $x/d = 20$ (relative to $x/d = 10$) and the correspondingly lower value of the (global) turbulent Prandtl number at that station (cf. §4). A possible explanation may be related to vortex A being further away from the centreline relative to $x/d = 10$ (e.g. the locations† of the centres in figure 8*b* relative to figure 8*a*) and therefore more influenced by the mean shear. A slight tilt of the vortices in the direction of the shear would result in a slight increase in $\tilde{u}\tilde{v}$ (positive) in quadrant II and a corresponding decrease in $\tilde{u}\tilde{v}$ (negative) in quadrant I. This is not inconsistent with the contours of figure 6(*b*). This explanation is similar to the net counter-gradient momentum transport suggestion of Hussain (1986) and could account for $\tilde{u}\tilde{v}$ being of opposite sign to $\overline{uv}$ in the region $1 \lesssim |y^*| \leqslant 2$ (figure 3*b*).

† These are in reasonable agreement with Hayakawa & Hussain's (1989) most probable locations of structure centres; the present magnitudes of the vortex convection velocity (Zhou & Antonia 1992) are in quite close agreement with the values reported by Hayakawa & Hussain.

7. Conclusions

Use has been made of the phase-averaging technique, previously developed by Kiya & Matsumura (1985, 1988), to quantify the contributions from the coherent motion to various Reynolds-averaged statistics, including the average momentum and heat fluxes. The results unequivocally indicate that the vortices transport heat more effectively than momentum, especially at $x/d = 10$ and 20. Consistent with this behaviour is the greater asymmetry, at these two stations, of the $\tilde{v}\tilde{\theta}$ contours relative to the $\tilde{u}\tilde{v}$ contours. This asymmetry reflects that in $\tilde{\theta}$, which is due to the presence of relatively colder fluid downstream of individual vortices and which contrasts with the near-symmetry of $\tilde{u}$.

There are substantial changes between $x/d = 10$ and 40 in the coherent momentum and heat fluxes. Smaller, but nonetheless important, variations are also observed in the incoherent fluxes. Contours of $\overline{u'v'}$ and $\overline{v'\theta'}$ exhibit reasonable similarity at $x/d = 40$, reflecting the similarity between $\overline{uv}$ and $\overline{v\theta}$ in figure 3. There is a change of sign and substantial variation in the magnitude of the longitudinal heat flux between $x/d = 10$ and 40.

The location of the maximum in $\bar{T} + \tilde{\theta}$ corresponds approximately to the location of the extremum in $\tilde{\omega}$ at all values of x/d. However, the close similarity between $\bar{T} + \tilde{\theta}$ and $\tilde{\omega}$ at $x/d = 10$ quickly impairs at larger x/d, implying that temperature becomes a less effective marker of the vortices as x/d increases. Within the vortices, the coherent heat flux vector is approximately aligned with the velocity vector, when the latter is viewed in a frame of reference which translates with the vortices. In the alleyway between vortices, the coherent heat flux vector is mainly in a direction opposite to the velocity vector.

R.A.A. acknowledges the support of the Australian Research Council. The comments on the manuscript by Y. Zhou and D. K. Bisset are much appreciated. We also acknowledge Y. Zhou's contribution to the experiments. Dr Matsumura's visit to the University of Newcastle was supported by the Ministry of Education, Science and culture of Japan.

REFERENCES

ANTONIA, R. A. 1991 Organization in a turbulent near-wake. *Fluid Dyn. Res.* **7**, 139–149.

ANTONIA, R. A. & BROWNE, L. W. B. 1986 Heat transport in a turbulent plane wake. *Intl J. Heat Mass Transfer* **29**, 1585–1592.

ANTONIA, R. A., BROWNE, L. W. B., BISSET, D. K. & FULACHIER, L. 1987 A description of the organized motion in the turbulent far-wake of a cylinder at low Reynolds number. *J. Fluid Mech.* **184**, 423–444.

BOISSON, H. C., CHASSAING, P. & HA MINH, H. 1983 Conditional analysis of intermittency in the near wake of a circular cylinder. *Phys. Fluids* **26**, 653–658.

CANTWELL, B. & COLES, D. 1983 An experimental study of entrainment and transport in the turbulent near wake of a circular cylinder. *J. Fluid Mech.* **136**, 321–374.

CIMBALA, J. M., NAGIB, H. M. & ROSHKO, A. 1988 Large structure in the far wakes of two-dimensional bluff bodies. *J. Fluid Mech.* **190**, 265–298.

FABRIS, G. 1979 Turbulent temperature and thermal flux characteristics in the wake of a cylinder. In *Turbulent Shear Flows 1* (ed. F. Durst, B. E. Launder, F. W. Schmidt & J. H. Whitelaw), pp. 55–70. Springer.

FERRÉ, J. A. & GIRALT, F. 1989 Some topological features of the entrainment process in a heated turbulent wake. *J. Fluid Mech.* **198**, 65–78.

FERRÉ, J. A., MUMFORD, J. C., SAVILL, A. M. & GIRALT, F. 1990 Three-dimensional large-eddy motions and fine-scale activity in a plane turbulent wake. *J. Fluid Mech.* **210**, 371–414.

HAYAKAWA, M. & HUSSAIN, F. 1989 Three-dimensionality of organized structures in a plane turbulent wake. *J. Fluid Mech.* **206**, 375–404.

HUSSAIN, A. K. M. F. 1983 Coherent structures – reality and myth. *Phys. Fluids* **26**, 2816–2850.

HUSSAIN, A. K. M. F. 1986 Coherent structures and turbulence. *J. Fluid Mech.* **173**, 303–356.

HUSSAIN, A. K. M. F. & HAYAKAWA, M. 1987 Eduction of large-scale organized structures in a turbulent plane wake. *J. Fluid Mech.* **180**, 193–229.

KIYA, M. & MATSUMURA, M. 1985 Turbulence structure in the intermediate wake of a circular cylinder. *Bull. JSME* **28**, 2617–2624.

KIYA, M. & MATSUMURA, M. 1988 Incoherent turbulence structure in the near wake of a normal plate. *J. Fluid Mech.* **190**, 343–356.

MATSUMURA, M., HUANG, Z., KAWALL, J. G. & KEFFER, J. F. 1991 Coherent structures in the turbulent wake of a porous body. In *Proc. Eighth Symp. on Turbulent Shear Flows, Munich*, pp. 28-2-1–28-2-5.

MUMFORD, J. C. 1983 The structure of the large eddies in fully developed turbulent shear flows. Part 2. The plane wake. *J. Fluid Mech.* **137**, 447–456.

REYNOLDS, W. C. & HUSSAIN, A. K. M. F. 1972 The mechanism of an organized wake in turbulent shear flow. Part 3. Theoretical models and comparisons with experiments. *J. Fluid Mech.* **54**, 263–288.

TOWNSEND, A. A. 1979 Flow patterns of large eddies in a wake and in a boundary layer. *J. Fluid Mech.* **95**, 515–537.

TRITTON, D. J. 1988 *Physical Fluid Dynamics*, 2nd edn. Oxford Science.

ZHOU, Y. & ANTONIA, R. A. 1992 Convection velocity measurements in cylinder wake. *Expts. Fluids* **13**, 63–70.